Biophysical *Journal*
Article

Biophysical Society

Active Site Flexibility as a Hallmark for Efficient PET Degradation by *I. sakaiensis* PETase

Tobias Fecker,[1] Pablo Galaz-Davison,[1] Felipe Engelberger,[1] Yoshie Narui,[2] Marcos Sotomayor,[2,*] Loreto P. Parra,[1,3,*] and César A. Ramírez-Sarmiento[1,*]

[1]Institute for Biological and Medical Engineering, Schools of Engineering, Medicine, and Biological Sciences, Pontificia Universidad Católica de Chile, Santiago, Chile; [2]Department of Chemistry and Biochemistry, The Ohio State University, Columbus, Ohio; and [3]Department of Chemical and Bioprocesses Engineering, School of Engineering, Pontificia Universidad Católica de Chile, Santiago, Chile

ABSTRACT Polyethylene terephthalate (PET) is one of the most-consumed synthetic polymers, with an annual production of 50 million tons. Unfortunately, PET accumulates as waste and is highly resistant to biodegradation. Recently, fungal and bacterial thermophilic hydrolases were found to catalyze PET hydrolysis with optimal activities at high temperatures. Strikingly, an enzyme from *Ideonella sakaiensis*, termed PETase, was described to efficiently degrade PET at room temperature, but the molecular basis of its activity is not currently understood. Here, a crystal structure of PETase was determined at 2.02 Å resolution and employed in molecular dynamics simulations showing that the active site of PETase has higher flexibility at room temperature than its thermophilic counterparts. This flexibility is controlled by a novel disulfide bond in its active site, with its removal leading to destabilization of the catalytic triad and reduction of the hydrolase activity. Molecular docking of a model substrate predicts that PET binds to PETase in a unique and energetically favorable conformation facilitated by several residue substitutions within its active site when compared to other enzymes. These computational predictions are in excellent agreement with recent mutagenesis and PET film degradation analyses. Finally, we rationalize the increased catalytic activity of PETase at room temperature through molecular dynamics simulations of enzyme-ligand complexes for PETase and other thermophilic PET-degrading enzymes at 298, 323, and 353 K. Our results reveal that both the binding pose and residue substitutions within PETase favor proximity between the catalytic residues and the labile carbonyl of the substrate at room temperature, suggesting a more favorable hydrolytic reaction. These results are valuable for enabling detailed evolutionary analysis of PET-degrading enzymes and for rational design endeavors aiming at increasing the efficiency of PETase and similar enzymes toward plastic degradation.

INTRODUCTION

Since its discovery in the 1940s (1), polyethylene terephthalate (PET) has emerged as one of the most-consumed synthetic polymers, with an annual production of nearly 50 million tons (2). Its durability, low permeability to gases, and transparency make PET an appealing product for the packaging market and textile industry (3). Although manufacturing this polymer is trivial, its characteristic longevity due to the chemical inertness of its aromatic compounds becomes disadvantageous during the recycling process, making it expensive and highly energy consuming (3). Moreover, PET accumulates as plastic waste in oceans at rates paralleling its production levels, thus constituting a rapidly increasing environmental threat (4).

The past few years have witnessed the discovery of several enzymes that catalyze PET hydrolysis and that are promising biocatalysts for environmentally friendly alternatives to chemical recycling (5,6). Such enzymes have been reported to exist in several saprotrophic or phytopathogenic organisms, including fungi (7–12) and bacteria (13–23), which usually inhabit environments enriched in plant-based organic matter or plastic debris and, in extreme cases, use PET as a main carbon source for cell growth (23). All known PET-degrading enzymes correspond to cutinases and carboxylesterases (6), which belong to the α/β-hydrolase superfamily and share a remarkably similar fold even with low sequence identity (24). This suggests that substitutions in key residues within the active sites led to the emergence of PET hydrolysis in PET-degrading enzymes.

Submitted October 24, 2017, and accepted for publication February 8, 2018.

*Correspondence: cesar.ramirez@uc.cl or lparraa@ing.puc.cl or sotomayor.8@osu.edu

Tobias Fecker and Pablo Galaz-Davison contributed equally to this work.

Editor: Bert de Groot.

https://doi.org/10.1016/j.bpj.2018.02.005

Extensive experimental evidence has demonstrated that both the mobility of the polymer chains and the accessibility of the enzyme's active site are the major factors enabling the biodegradability of PET (25–29). Enzymatic PET hydrolysis increases with temperature because of a higher probability of surface chains leaving the polymer structure near its glass transition temperature ($T_g = 65°C$), becoming available targets that fit into the active site of PET-degrading enzymes (26). Therefore, most of these enzymes preferentially hydrolyze amorphous regions of PET, where its chain mobility is less restricted than in highly crystallized regions (28). Likewise, most known PET-degrading enzymes come from thermophilic organisms whose optimal activities are near such T_g (14–17,19–21,30), or that have been engineered through rational design to increase their thermostability and exceed this critical temperature, thus improving activity toward this substrate (22,31–34). On the other hand, a higher accessibility or exposure of the active site on the protein surface for substrate binding is known to increase polyester hydrolysis (29) by compensating for the high T_g of some polymers like PET (26). Numerous engineering efforts have successfully exploited the enlargement of the active sites of several PET-degrading enzymes to increase their plastic-degrading activity (35–37), but in all cases high temperatures are still required for efficient PET hydrolysis.

Recent work by Yoshida et al. (23) described for the first time the bacterial species *Ideonella sakaiensis* 201-F6, which is able to use PET as its primary carbon source by the activity of a novel PET hydrolase that efficiently breaks down this polyester at moderate (mesophilic) temperatures, between 20 and 40°C. This enzyme, termed PETase, showed between 5 and 120 times higher depolymerization activity against PET films at 30°C than thermophilic PET-degrading enzymes tested to date.

The fact that PETase can degrade PET films at room temperature contrasts with the need of high temperature to facilitate PET hydrolysis by other hydrolases, hence raising questions regarding the structural and sequence features that allow PETase to outperform its homologs at lower temperatures. In addition, PET film degradation experiments show that PETase reaches maximum activity at lower protein concentrations than other thermophilic PET-degrading enzymes, thus suggesting a tighter binding to this plastic substrate (23). These arguments raise the need for a deeper understanding of the binding interactions of PETase to this polymer.

In this work, we used a combination of structural biology and computational modeling to get insights into the structure and sequence features enabling the high activity of PETase at room temperature. First, we solved the crystal structure of PETase at 2.02 Å resolution. Then, we performed comparative molecular dynamics (MD) simulations of our novel structure and two other prominent PET-degrading cutinases with solved structures: TfCut2 from *Thermobifida fusca*, and a leaf-branch compost cutinase (LCC) from metagenomes. All three cutinases show high sequence identity and structural similarity, yet PETase exhibits a novel disulfide bond near the active site and higher flexibility within loops contributing the enzyme's catalytic residues. Enzyme kinetics under reducing conditions and MD simulations in the absence and presence of the active site's disulfide bond demonstrate that this covalent interaction is important for maintenance of the active site integrity and catalytic activity. Finally, comparative molecular docking of a model substrate comprising two repeating units of ethylene terephthalate (2PET), followed by MD simulations of the enzyme-substrate complex, predict that several residue substitutions are responsible for improved PET binding and reveal a different binding conformation that enables a more favorable interaction distance between the target PET backbone ester and the PETase catalytic residues. Our results constitute an important step in guiding future rational design of PETase and other cutinases toward higher PET degradation efficiency at room temperature.

MATERIALS AND METHODS

Protein expression and purification of PETase

The codon-optimized gene for PETase from *I. sakaiensis* strain 201-F6 without signal-peptide (Genscript, Piscataway, NJ)—identified using SignalP (DTU Bioinformatics, Kongens Lyngby, Denmark) (38)—was synthesized, cloned into a pET24b vector (EMD Biosciences, Madison, WI), and transformed into *Escherichia coli* BL21-Gold(DE3) (Agilent Technologies, La Jolla, CA). Bacteria were grown in Terrific Broth (Thermo Fisher Scientific, Waltham, MA), and protein expression was induced for 18 h at 25°C using 1.0 mM isopropyl β-D-1-thiogalactopyranoside after reaching an optical density at 600 nm of 0.7. Cells were harvested by centrifugation, then lysed by sonication in denaturing buffer containing 6 M guanidine hydrochloride and 50 mM sodium phosphate (pH 7.5). Cleared lysates containing His-tagged PETase were loaded onto Ni-Sepharose (GE Healthcare Bio-Sciences, Pittsburgh, PA), washed twice with lysis buffer, and then eluted using 350 mM imidazole. Protein was refolded by overnight dialysis at 4°C against buffer containing 400 mM L-arginine, 50 mM sodium phosphate (pH 7.5), and 150 mM NaCl. The refolded protein was further purified by size-exclusion chromatography on a Superdex75 column (GE Healthcare) in buffer containing 50 mM sodium phosphate (pH 7.5) and 90 mM NaCl. The fractions corresponding to a monodisperse peak were assayed and visually inspected through SDS-PAGE (Fig. S1).

Crystallization, data collection, and structure refinement

Pure active protein was concentrated by ultrafiltration and used for crystallization trials using the sitting drop vapor diffusion method at 4°C with a mixture at a 1:1 ratio of protein ($\sim$7 mg·mL^{-1}) and reservoir solution. PETase crystals were obtained in reservoir solution containing 0.1 M MES (pH 6.5) and 1.6 M $MgSO_4$. Crystals were cryoprotected in reservoir solution containing 20% glycerol and flash-frozen in liquid N_2. X-ray diffraction data was obtained using a Rigaku Micromax-003 X-ray source (Rigaku Americas, The Woodlands, TX) and a Dectris Pilatus 200K detector (Dectris, Baden-Dättwil, Switzerland). Data were collected as indicated in Table 1 and further processed using HKL-2000 (HKL Research, Charlottesville, VA) (39). The structure was solved by molecular replacement with

TABLE 1 Statistics for PE Tase Structure (PDB: 6ANE)

Data Collection	
Space Group	C 2 2 21
Unit Cell Parameters	
a, *b*, *c* [Å]	52.87, 233.85, 165.08
α, β, γ [°]	90, 90, 90
Molecules per asymmetric unit	3
Detector	Dectris Pilatus 200K
X-ray source	Rigaku Micromax-003
Wavelength [Å]	1.5418
Resolution range [Å][a]	116.93–2.02 (2.05–2.02)
Total reflections	2,046,244
Unique reflections[a]	67,721 (3,054)
Redundancy[a]	6.0 (3.9)
Completeness [%][a]	95.9 (92.4)
I/σ [I][a]	9.83 (2.0)
R_{meas} [%]	0.114 (0.750)
Refinement	
Reflections used for refinement	61,680
R_{work} [%]	17.7
R_{free} [%]	21.7
Residues [atoms]	787 (5808)
Water molecules	474
Model Quality	
RMSDs	
Bond length [Å]	0.013
Bond angles [°]	1.508
B-factor average	
Protein	21.63
Ion	23.98
Water	26.57
Ramachandran Plot Region	
Favored [%]	98
Allowed [%]	2
Outliers [%]	0

[a]Statistics for the highest resolution shell are shown in parenthesis.

Phaser (McCoy et al., Cambridge, England) (40), using the crystal structure of TfCut2 as template (Protein Data Bank (PDB): 4CG1 (41)), and further refined using Refmac (Computational Crystallography Group, Cambridge, England) (42) and Coot (Emsley et al., Cambridge, England) (43). The structure was deposited in the Protein Data Bank under accession PDB: 6ANE.

Kinetic assays

Activity was measured by spectrophotometrically following the hydrolysis of *p*-nitrophenyl acetate (*p*NPA; Sigma-Aldrich, St. Louis, MO) into acetate and *p*-nitrophenol. This was performed at room temperature in buffer containing 50 mM sodium phosphate pH (7.5) and 90 mM NaCl, with less than 4% v/v dimethyl sulfoxide from the *p*NPA stock solution. Size-exclusion chromatography-purified PETase was incubated in the presence or absence of 10 mM Tris(2-carboxyethyl)phosphine hydrochloride (TCEP) for 10 min at room temperature prior to initiation of the enzymatic reaction, and 25 nM of PETase were used per pNPA assay. Protein concentration was calculated prior to and following the assay and no difference was found.

The production of *p*-nitrophenolate was measured at 405 nm ($\varepsilon_{405} = 18{,}400\ \mathrm{nm}^{-1}\cdot\mathrm{M}^{-1}$ (44)), including its equilibrium toward the acidic *p*-nitrophenol (45). Nonenzymatic *p*NPA hydrolysis initial rates were measured, fitted to a pseudo-first-order kinetics model, and subtracted from enzymatic activity, which was further fitted using a Michaelis-Menten model.

MD simulations

Explicit-solvent MD simulations were performed using the crystal structures of TfCut2 (PDB: 4CG1 (41)), LCC (PDB: 4EB0 (30)), and PETase (PDB: 6ANE, chain B). Simulations were carried out using the Amber16 suite (Amber Software, San Francisco, CA) (46) along with the AMBERff14SB force field (47). For each system, a simulation system with 1.5 nm of padding was filled with TIP3P water molecules and neutralized with counter ions (Table S1). Each system was minimized using the steepest descent method and then equilibrated at 298 K for 150 ps at constant volume using a Langevin thermostat, followed by equilibration for 1 ns at a constant pressure of 1 bar using a Berendsen barostat until density was stable. Production MD runs were carried out in three replicas for 50 ns each, using a timestep of 2.0 fs alongside the SHAKE algorithm and particle mesh Ewald method for long range electrostatics, with a 10 Å cutoff for short-range electrostatics. For each system, replicas were checked for structural convergence using the overall backbone root mean-square deviation (RMSD) from the first frame of the respective trajectory and for integrity of the configuration of the catalytic triad, particularly the interaction between Ser and His. For PETase, simulations were performed both in the presence and in the absence of both disulfide bonds, or in the absence of the active site's disulfide bond.

Parameterization and molecular docking of a model PET substrate

A model substrate consisting of two consecutive units of 2PET was parameterized for molecular docking in Rosetta3 (RosettaCommons) (48). First, 2PET was constructed and minimized using Avogadro (Avogadro Chemistry) (49) and parameterized using the Antechamber module of Amber16 (Amber Software) (50) along with the General AMBER force field (51) and the AM1-BCC charge model (52). To extensively explore the possible binding poses of 2PET, 277 conformers were created using the confab package of Open Babel (53), based on an RMSD cutoff of 1.3 Å and an energy cutoff of 50 kcal/mol. Then 10,000 enzyme-substrate complex structures were generated by docking 2PET onto the binding site of the crystal structures of TfCut2, LCC, and PETase using a custom Rosetta3 (RosettaCommons) XML script enabling backbone and side-chain flexibility as previously described (54). To ensure correct orientation of the substrate, the carbonyl oxygen of the ester group was restrained to the two backbone nitrogen atoms forming the enzymes' oxyanion hole with a flat harmonic potential between 1.5 and 3.5 Å. The lowest 10% energy-scoring complexes were clustered using a ligand RMSD cutoff of 2 Å, and the lowest-energy enzyme-substrate complex from the most populated cluster was further used for MD simulations. The substrate *p*NPA was docked onto PETase using the same protocol.

The binding energy and per-residue decomposition of the energetic contributions were extracted from the top 10% scoring poses of the most populated cluster generated in the previous step using Rosetta's DDG mover as previously described (55).

MD simulations of PETase bound to 2PET

Each lowest-energy enzyme-2PET complex was parameterized using the AnteChamber module of Amber16 (Amber Software) (50) and simulated in triplicates for 10 ns as described above for the free enzymes (Table S1). The relative frequency distribution of the catalytic distance was determined by measuring the minimum distance of any substrate carbonyl atom to the hydroxy-oxygen of the catalytic serine. Samples were taken for the

last 5 ns of all simulations, collecting frames every 5 ps (1000 frames sampled per simulation). To investigate the temperature dependence of the catalytic distance, simulations were performed at 298, 323, and 353 K for all complexes.

Additionally, PET binding free energies were calculated using the single trajectory approach of the molecular mechanics combined with generalized Born and surface area method (56) in Amber16 (46). The estimated binding free energies correspond to the average values from three independent simulations at 298 K.

RESULTS AND DISCUSSION

Novel structural features of PETase

To understand the structural basis of enhanced PET-degrading activity at room temperature, we expressed, purified (Fig. S1), and crystallized PETase from *I. sakaiensis* (UniProt: A0A0K8P6T7). A diffraction data set collected using an in-house x-ray source was processed and phased by molecular replacement using the homologous thermophilic PET-degrading cutinase TfCut2 from *T. fusca* (percentage identity = 51%; PDB: 4CG1 (41)). The initial structural model was refined to a final R_{work}/R_{free} = 17.7/21.7 (Table 1), with three molecules of the enzyme and a magnesium ion in the asymmetric unit. The crystallographic structure shows all but the initial glutamine residue of the signal peptide-excised enzyme (Fig. 1, *A* and *B*).

The overall topology of PETase is similar to that of other α/β hydrolases, with six α-helices and nine β-strands that follow the architecture of its closest structural homologs TfCut2 and LCC (percentage identity = 49%; PDB: 4EB0 (18)). The secondary structure remains mostly the same among the three enzymes, yet slight differences exist: there is an extra turn extension in helix α2 of PETase because of a three-residue insertion, followed by the absence of a short α-helix between α2 and β5. Two 3_{10}-helices are missing: one between β1 and β2 is absent because of a Leu to Pro substitution at position 44 followed by a two-residue deletion, whereas the other would be located in proximity to the active site in the loop connecting β-strand β8 and helix α5 (Fig. 1 *C*). A C-terminal disulfide bond (C246-C262) connecting the final helix α6 and β-strand β9 that is thought to play a crucial role in the stability of cutinases (30,41) is also present in PETase (Fig. 1 *A*).

Interestingly, PETase has a second disulfide bond (C176-C212) formed by two cysteine residues that correspond to highly conserved alanines in other cutinases. This bond links a buried site in β-strand β7, right below the enzyme's active site, to a loop connecting β-strand β8 with helix α5, where the aforementioned 3_{10}-helix is missing (Fig. 1 *A*). The first half of this loop, with a backbone that can be structurally overlapped among the three enzymes, bears the catalytic histidine residue (His 210) and is tightly anchored by the C176-C212 disulfide bond. In contrast, a three-residue-long insertion in the other half of the loop connecting strand β8 with helix α5 displaces part of the loop and the subsequent α5 helix away from the active site when compared to the thermophilic cutinases. Thus, the novel disulfide bond may allow for a longer and more flexible loop to exist within the active site without compromising structural and catalytic integrity.

The identity and orientation of residues forming the active site of PETase display a few remarkable differences when compared to its thermophilic counterparts: although the catalytic triad composed of S133, H210, and D179 is strictly conserved and their side chains share the same orientation in all structures (Fig. 1 *B*), there are at least three changes in the amino acid identity of neighboring residues that might be relevant for function. First, there is a substitution of a histidine residue (conserved in other cutinases) by a more hydrophobic tryptophan residue at position 132. Second, there is a change from a conserved phenylalanine to serine at position 211. Lastly, there is another change of a conserved histidine residue to serine at position 187 (Fig. 1 *B*). In addition, and despite being structurally conserved, unambiguous assignment for the conformation of the side chain of W158 near S133 was not possible in chains B and C (Fig. 1 *B*). This was characterized as a wobbly tryptophan in a recent work with PETase (57), in which they observe all three conformers of this residue. Overall, these amino acid substitutions and their side-chain orientations modify the environment of the catalytic triad, widening the ends of the binding cavity (Fig. S2) and likely contributing to the enhanced activity of PETase.

Molecular docking reveals a distinct PET binding pose on PETase

To understand how PETase binds and hydrolyses PET, we used a custom Rosetta3 protocol (RosettaCommons) (54) that takes into account flexibility in both macromolecule and ligand to model a substrate consisting of a dimer of 2PET docked onto the crystal structures of PETase, TfCut2, and LCC. These enzymes exhibit the highest reported PET-degradation activities to date (18,23,33), and 2PET is a good substrate model since the hydrolysis rate of its analog molecule bis(hydroxyethyl) terephthalate (BHET) is well-correlated with the degradation of PET films and can thus be used to estimate the enzymatic surface hydrolysis of the polymer (58).

The resulting conformations for the lowest-energy enzyme-substrate complexes are shown in Fig. 2. The carbonyl oxygen of the substrate's ester group was placed close to the backbone amide nitrogen of the oxyanion hole in all proteins, where the transition state is stabilized during the deacetylation/acetylation reaction (59) and which is in close proximity to the catalytic residues that enable the initiation of the reaction.

Similar to other cutinases, the active site crevice of PETase displays a kink of roughly 45° with an aromatic clamp formed by W158 and Y60 (41), which anchors the terephthalic ring inside the active site in a highly bent

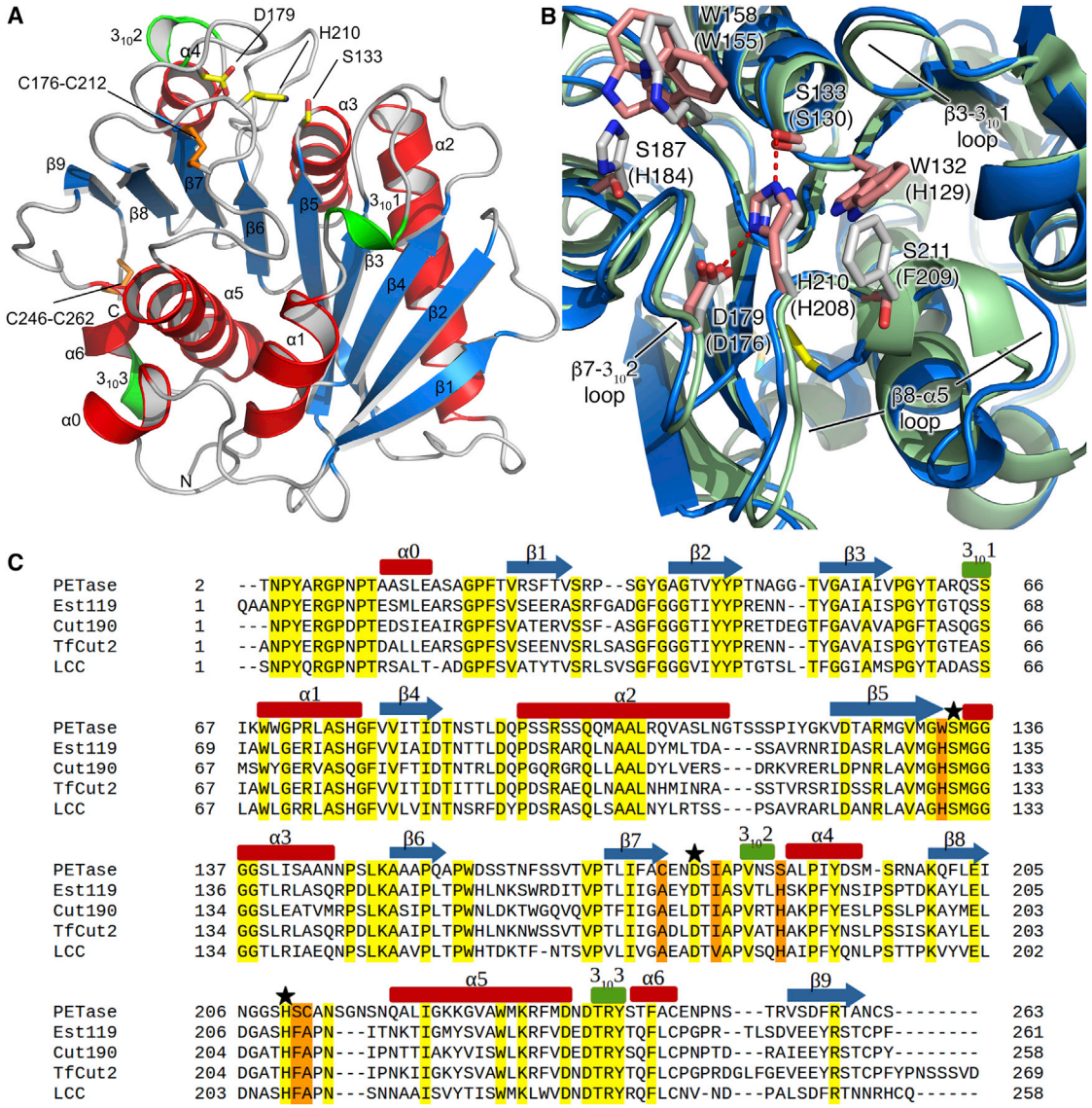

FIGURE 1 Crystal structure of PETase and comparison to other PET-degrading cutinases. (*A*) Shown here is a cartoon representation of the overall structure of PETase (PDB: 6ANE, chain B), with secondary structure elements of the α/β-hydrolase depicted in blue and red for β-strands and helices, respectively, and 3_{10}-helices in green. Residues of the catalytic triad are shown as yellow sticks, and disulfide bridges are shown in orange. (*B*) Shown here is a comparison between the active sites of PETase *(blue)* and TfCut2 (*green*, PDB: 4CG1). The catalytic triad and neighboring residues that are distinct in PETase but conserved in other cutinases are displayed in pink (PETase) and white (TfCut2) sticks. Residues are labeled according to their PETase numbering, with TfCut2 numbering in parenthesis. The disulfide bond between residues C176-C212 in PETase is shown in yellow sticks. (*C*) Shown here is the structure-based sequence alignment of PETase and other PET hydrolases: LCC (PDB: 4EB0), Est119 (PDB: 3VIS), TfCut2 (PDB: 4CG1), and Cut190 (PDB: 4WFJ). The secondary structure for PETase is shown above the alignment, and catalytic residues are marked with a star. Conserved residues are highlighted in yellow; major changes in sequence between PETase and its homologs are highlighted in orange. To see this figure in color, go online.

conformation (Fig. 2 *A*). This conformation roughly resembles the binding pose predicted by Kawabata et al. (60) between an aromatic substrate consisting of varying terephthalate and ethylene moieties and Cut190, as well as the crystal structure of the PEG-Est119 complex (61). Interestingly, the 2PET substrate is bound in a more straightened conformation in the active site of both LCC and TfCut2 (Fig. 2, *B* and *C*), as has been previously reported for TfCut2 (37,41) and also for Tcur1278 and Tcur0390, cutinases from *Thermomonospora curvata* (21). The observed binding pose is a consequence of the elongated active site groove of LCC and TfCut2, as opposed to the relatively short crest in PETase because of the F211S substitution in the vicinity of its active site (Fig. 2 *A*).

To analyze the interactions involved in each of the predicted binding poses, we estimated free-energy changes (on an arbitrary Rosetta energy unit scale) of individual residues upon substrate binding for the three complexes (Fig. 2 *D*). Since this estimation does not provide physical values for evaluating the free energy of ligand binding

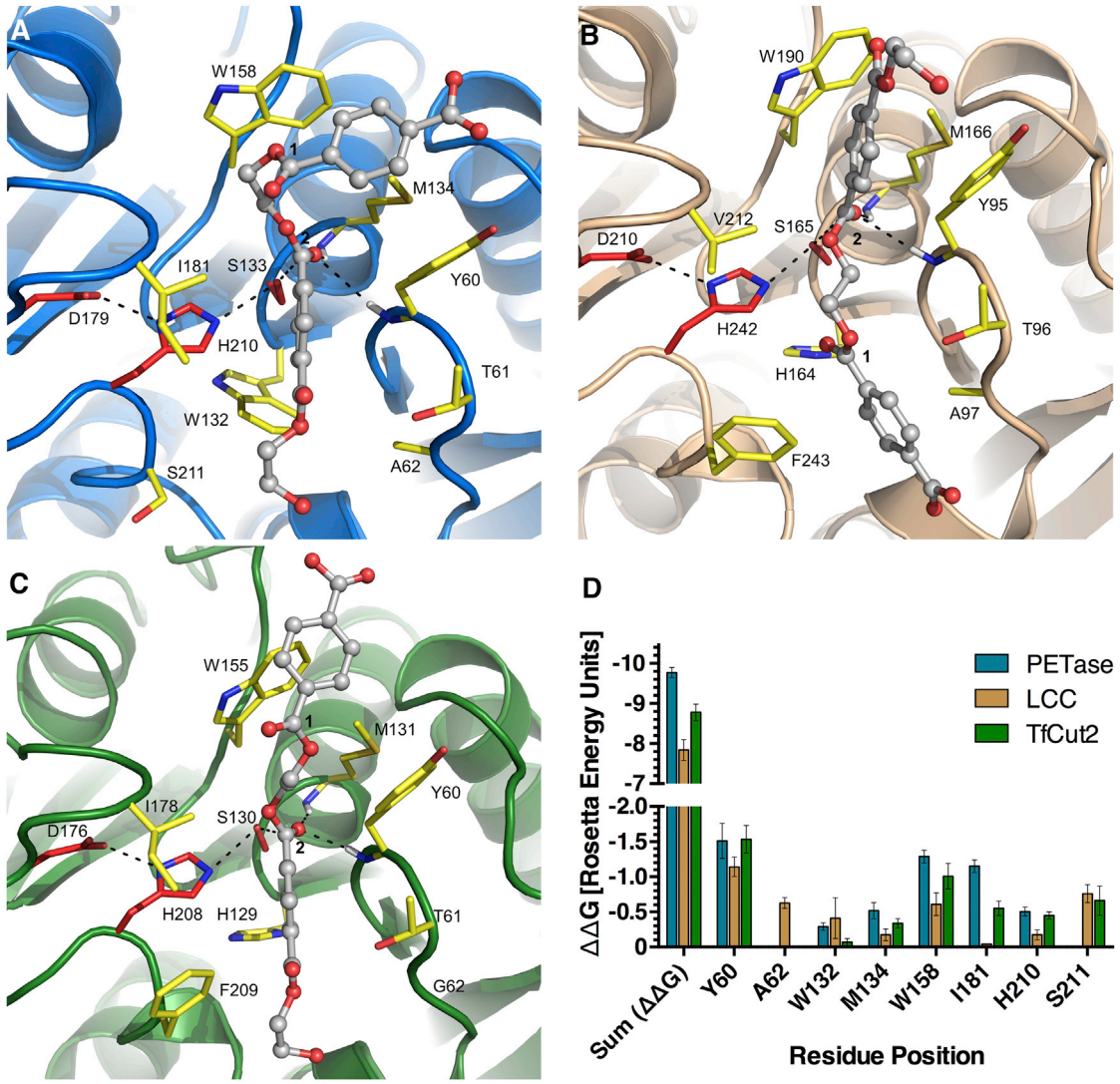

FIGURE 2 Predicted binding pose of a model PET substrate into the active site of PETase and other PET-degrading cutinases. (*A–C*) Shown here are cartoon representations of PETase (*A*), LCC (*B*), and TfCut2 (*C*) in complex with the model substrate 2PET. The substrate is shown in ball and sticks, the catalytic triad is colored in red sticks, and other residues involved in binding (based on Rosetta prediction) are shown in yellow. Labile ester bonds within PET are numbered from the terephthalic free end. Interactions between the substrate and the catalytic serine as well as with the residues of the oxyanion hole are shown in black dashed lines. (*D*) Given here are the estimated per-residue free energy contributions (ΔΔG) to the calculated substrate binding for PETase and its homologs LCC and TfCut2 predicted by Rosetta (54), shown as average ± standard deviation. Residue numbering corresponds to the equivalent position for each enzyme on the sequence of PETase. To see this figure in color, go online.

(62), we performed molecular mechanics combined with generalized Born and surface area calculations, obtaining per-residue energy contributions that follow the same trend as our estimations from molecular docking with Rosetta (Fig. S2 *D*). Consistently, interactions between residues of the aromatic clamp (W158 and Y60) and the terephthalic ring in the substrate contribute significantly and with similar magnitude to the overall ΔΔG (~15% of the total binding energy for each residue) in all three enzyme-substrate complexes. Recent work showed that alanine substitutions of these residues in PETase reduced BHET and PET film hydrolysis by more than 90% (57,63).

One of the main differences in the contributions from active site residues to binding of 2PET corresponds to residue I181 in PETase, which is responsible for 12% of the global binding energy according to Rosetta. In contrast, residues in equivalent sites of LCC (Val) and TfCut2 (Ile) do not significantly contribute to 2PET binding. Recent experimental characterization of PETase revealed that an alanine substitution in this position consistently and significantly reduces PET film hydrolysis between ~80% (57) and ~60% (63). The aromatic ring of 2PET interacts with the phenylalanine side chain at the entrance of the binding cavity in both LCC (F243) and TfCut2 (F209), whereas the equivalent serine residue (S211) in PETase does not

interact with the polymer, and indeed an alanine substitution of this residue does not dampen BHET or PET film hydrolysis (63). On the other end, the flexible W158 side chain remains pushed away from the active site of PETase, thus giving the 2PET molecule enough room to adopt this crooked conformation. To a lesser extent, the conserved residue M134, which contributes 5% of the total binding ΔΔG, also seems to favor PET binding by contributing to the hydrophobic environment around its terephthalic ring. In fact, alanine substitutions in this position lead to a decrease of half of its BHET hydrolysis activity (63) and ~80% of its PET film degradation activity (57).

Although several active site residues, such as Y60, M134, and W158, are conserved and equally contribute to the PET binding energy as well as playing an important role in PET hydrolysis (57,63), they do not contribute to elucidating the determinants of the enhanced activity of PETase at room temperature. Moreover, there are a few substitutions of conserved bulky residues with smaller side chains (i.e., S211 instead of a conserved phenylalanine) that might play an important role in increasing the size of the active site crevice and its flexibility. All these subtle yet key differences between the conformation and protein-substrate interactions found among the catalytic complexes, along with changes in active site flexibility, may give rise to the enhanced PET hydrolysis seen experimentally for PETase at room temperature.

MD simulations predict increased active site dynamics and enhanced binding in PETase

To explore how structural differences and substrate binding affect active site dynamics in PETase, TfCut2, and LCC, all three free enzymes were solvated and simulated without substrate (APO) in triplicates for 50 ns each. Analysis of MD simulation trajectories revealed significant backbone root mean-square fluctuation (RMSF) in the loops connecting β-strand β3 with its following helix $3_{10}1$ (residues 57-64), β-strand β7 with helix $3_{10}2$ (residues 176-184), and β-strand β8 with helix α5 (residues 205-220; Fig. 3). Interestingly, average RMSF values were higher for PETase across the β7-helix $3_{10}2$ loop that bears the catalytic D179 residue (Fig. 2 *A*). The average RMSF for this region in PETase was 0.80 ± 0.20 Å, whereas the average RMSF values for LCC and TfCut2 in the same region were 0.56 ± 0.02 Å and 0.52 ± 0.01 Å, respectively (Table S2). The high backbone mobility of the D179-bearing loop in PETase hints at flexible areas within its active site that would enable binding of low-flexibility PET polymer chains at moderate temperatures.

Triplicates of 10-ns-long MD simulations of the enzyme-2PET complexes were produced to assess these flexibility changes upon substrate binding. All simulations started from catalytic complexes, i.e., the lowest energy conformations at which the 2PET labile carboxyl is at close distance

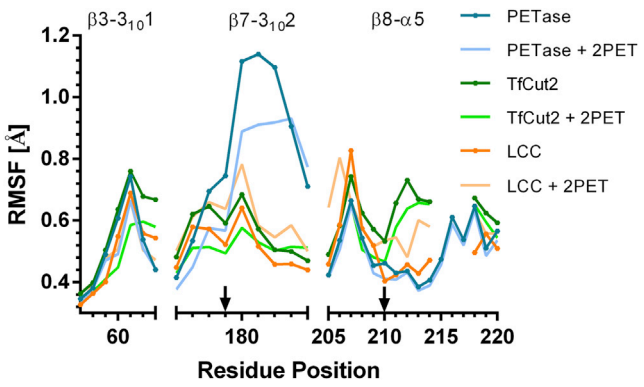

FIGURE 3 MD simulations reveal increased flexibility in the active site of PETase. Shown here are the average backbone RMSFs for the binding sites of PETase (*blue*), LCC (*orange*), and TfCut2 (*green*), with (*light color*) and without substrate (*dark color*). Loops within the active site were identified and compared among enzymes based on the sequence alignment shown in Fig. 1 *C*. All residue positions are numbered according to PETase sequence, and the catalytic Asp and His are marked with arrows. To see this figure in color, go online.

from the catalytic serine and correctly oriented by interactions with the oxyanion hole (Fig. 2). These simulations reveal that the loop connecting the β-strand β7 and helix $3_{10}2$ in the active site of PETase undergoes a drastic reduction in flexibility upon 2PET binding (Fig. 3), yet it remains the highest of the set. This same region bears the residue I181, which is involved in substrate binding only in PETase (Fig. 2 *D*). This is consistent with the mutation experiments of Kawabata et al. (60), in which the corresponding I224 residue mutated to alanine led to decreased affinity toward a similar hydrophobic substrate in Cut190. A global reduction in RMSF after binding is also noted for TfCut2, suggesting that both enzymes become locally stabilized by the presence of PET-like substrates in its active site. An opposite behavior is noted for LCC, whose fluctuations rise after the 2PET molecule is bound on its active site (Table S2). The latter suggests that not all interactions formed upon binding of 2PET onto the active site of LCC are stabilizing at this temperature, thus explaining its increase in flexibility.

To further understand how active site flexibility may correlate with the catalytic activity of PETase, LCC, and TfCut2, we measured the distance between the substrate's labile carbonyl and the catalytic serine during our MD simulations (Fig. 4), arguing that the smaller the distance, the higher the probability for a reaction to take place (59). Concomitantly, a Gaussian fit of the data recalls its reported activity (23): at room temperature (298 K), PETase keeps the reactive cores at 3.8 ± 0.7 Å, whereas LCC and TfCut2 do it a bit further away at 4.2 ± 0.5 and 4.5 ± 0.3 Å, respectively. Upon increasing the temperature to 323 K, PETase increases its mean distance to 4.4 ± 0.6 Å, whereas both LCC and TfCut2 maintain their distance at 4.1 ± 0.5 and 4.8 ± 0.4 Å, respectively.

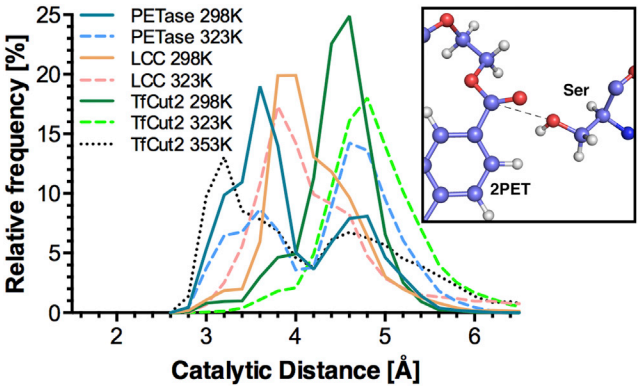

FIGURE 4 Histogram of catalytic distances for all enzyme-substrate complexes. The catalytic distance (inset) between the carbonyl carbon of 2PET and the oxygen of the catalytic serine of PETase (*blue*), LCC (*orange*), and TfCut2 (*green*) was monitored throughout MD simulations at three temperatures, 298 K (*solid lines*), 323 K (*dashed lines*), and 353 K (*dotted line*), respectively. Frames were taken every 5 ps from 10 ns trajectories generated by MD simulations of the previously docked complexes, and a distance bin size of 0.1 Å was used. To see this figure in color, go online.

Further increasing the temperature to 353 K results in substrate drifting away from the binding site for both PETase and LCC, whereas TfCut2 shows a reduction of the catalytic distance to 3.9 ± 1.2 Å.

Role of C176-C212 disulfide bond in enzyme kinetics and active site integrity

Enzymatic assays were performed for PETase with the small substrate *p*NPA, which, although it does not display the same chemical moieties as PET, binds to this enzyme in the same manner as a PET-like substrate (57). To explore the effects of breaking the disulfide bonds throughout the enzyme, *p*NPA hydrolysis kinetics were also performed after incubation in the presence of TCEP incubation (Fig. 5), with control experiments confirming that nonenzymatic hydrolysis of *p*NPA was similar in the presence and absence of this reducing agent (Fig. S3). Upon cysteine reduction, a decrease in V_{max} of nearly 30% was observed (from 31.3 ± 1.1 to 22.6 ± 1.1 U), whereas the affinity remained within range in both cases (K_M ~2.8 mM). To further explore this scenario, triplicates of 50-ns-long MD simulations of PETase with completely or partially reduced disulfides were carried out (Fig. S4), revealing that breaking the disulfide bond located within the active site is sufficient to compromise the integrity of the catalytic triad, as revealed by the change in mean distance between hydrogen-bonding atoms in the charge relay (Table 2).

In addition, PETase variants C176A, C212A, and C176A-C212A were expressed, purified and tested for enzymatic activity with *p*NPA. These variants showed insignificant hydrolysis of *p*NPA (Fig. S5). Furthermore,

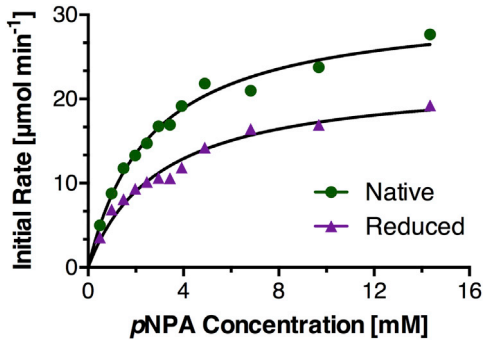

FIGURE 5 PETase kinetics for *p*NPA hydrolysis under native and reducing conditions. Enzymatic hydrolysis of *p*NPA by size-exclusion chromatography-purified PETase in the presence or absence of 10 mM TCEP. The parameters obtained after fitting the data to the Michaelis-Menten model are V_{max}: 31.3 ± 1.1 U and K_M: 2.6 ± 0.3 mM in native conditions, and V_{max}: 22.6 ± 1.1 U and K_M: 3.0 ± 0.4 mM in reducing conditions. To see this figure in color, go online.

recent work showed that serine substitutions of each individual cysteine resulted in little to no activity for PET film hydrolysis (57), whereas an alanine substitution abrogates BHET hydrolysis and reduces its activity around 80% in PET films (63). Taken together, these results highlight the essential role played by the C176-C212 disulfide bond in PETase activity.

CONCLUSIONS

Here we presented a crystal structure of PETase, an enzyme from *I. sakaiensis* 201-F6 that is able to degrade PET at mesophilic temperatures (23). We used this novel structure, along with two other reported crystals belonging to thermophilic PET-degrading cutinases, to model substrate (2PET) binding and carry out MD simulations that explored the dynamics of their active sites in APO and complexed forms. Our analyses and simulations revealed key structural determinants that may contribute to the enhanced PET-hydrolase activity of this enzyme when compared to its thermostable homologs.

PETase features a unique disulfide bond (C176-C212), variations in secondary structure, and fewer voluminous residues in its active site. Although disulfide bonds are typically associated with increased rigidity and thermal stability, PETase is somewhat thermal labile (23), and indeed our simulations in both its APO and complexed forms predict that flexibility in the loop connecting β-strand β7 with helix $3_{10}2$ (i.e., around the active site and bearing the catalytic D179 residue) is larger in PETase than in its closely related thermostable cutinases. When these cysteines are reduced, active site fluctuations increase dramatically and destabilize the integrity of the catalytic triad, leading to a decrease in enzymatic activity. Recent work showed that alanine substitutions of these cysteines reduces the melting temperature of PETase from 46.8 to 33.6°C (63), which

TABLE 2 Mean Hydrogen-Bond Distance between Catalytic Residues on PETase under Different Reduced/Nonreduced Disulfide Bond Simulation Conditions

	Hydrogen-Bond Mean Distance [Å]	
Status of Disulfide Bonds	D179-H210	H210-S133
Native	1.9 ± 0.2	3.1 ± 0.3
C176–C212 Reduced	2.3 ± 0.4	3.5 ± 0.3
Reduced	2.4 ± 0.4	3.8 ± 0.5

further emphasizes the idea that this enzyme is at the brink of instability—as its host is normally grown at 30°C (23)—and that the disulfide bond within the active site aids in keeping the integrity of the catalytic triad while allowing a higher flexibility in PETase than in the thermophilic counterparts.

Computational and experimental evidence thus supports the structural role of the C176-C212 disulfide bond in keeping the active site flexible enough to compensate for substrate rigidity without compromising the enzyme's structural integrity. Such active site flexibility has been predicted to play a major role in efficient PET hydrolysis, acting against product accumulation (64) and enabling conformational "breathing" dynamics of the active site for rapid binding to rigid substrates (65). Consistently, high fluctuations in the same loop have been reported using crystallographic data and MD simulations at 80°C for PET-degrading cutinases from *T. curvata* (21) and *T. fusca* (41). We propose that high flexibility of PETase loops at room temperature enables this enzyme to bind and degrade PET more efficiently than other cutinases.

Interestingly, catalytic complexes of all three enzymes share similar predicted energy toward PET binding as assessed by Rosetta, yet MD simulations of such complexes unequivocally show differential behavior toward this complex stabilization: although PETase is very likely to keep this conformation over time at 298 K, the distance between the substrate's reactive core and the catalytic serine increases upon heating at 323 K, whereas the substrate drifts away when the temperature is further increased to 353 K. A similar behavior is observed for LCC, although substrate binding does not seem to stabilize the active site, and the catalytic distance is not strongly influenced by temperature. In contrast, a shortening in the catalytic distance upon increasing the temperature is observed for TfCut2.

In this work, we predict that the hydrophobic W132 buried beneath the active site of PETase contributes little to the binding of 2PET, yet its substitution with alanine by Joo et al. (63) leads to a decrease of roughly 90% in BHET hydrolysis and around 80% when using PET films. We hypothesize that this effect may be due to changes in active site dynamics rather than affinity, as its voluminous side chain lays tightly packed between loops $\beta 3$-$3_{10}1$ and $\beta 8$-$\alpha 5$ (Fig. 1 *B*). Its removal may well lead to increased and excessive fluctuations in neighboring regions, particularly in the loop $\beta 8$-$\alpha 5$ bearing the catalytic H210, which would lead to reduced activity when the catalytic triad is compromised, as observed in our MD simulations with reduced disulfide bonds.

The binding mode of the substrate on PETase presented here is different from that recently suggested based on crystal structures of PETase with substrate and product analogs (57). This difference might arise from the different complexities of the substrate analogs employed: the 2PET molecule used here exposes three labile ester bonds and two aromatic rings, whereas the cocrystallized substrate 1-(2-Hydroxyethyl) 4-methyl terephthalate presented in (57) is more similar to *p*NPA in that it only exposes a single aromatic ring. Indeed, when docking *p*NPA using the same protocol described above, the resulting configuration of protein side chains is almost identical to that of the crystal structure solved with a substrate analog (PDB: 5XH3), and the substrate is bound in the same orientation (Fig. S6). It is worth noting that the energetic contributions derived from our computational work are highly consistent with recent experimental evidence on the role of several active site residues on the hydrolytic activity of PETase at room temperature (57,63). Hence, our work establishes a computational framework upon which further residue substitutions that aim to increase PETase activity can be explored.

Altogether, our data suggest that subtle residue variations within the sequence of PETase lead to drastic changes in overall dynamics, which supports the idea that key substitutions within the active site of this α/β hydrolase family are sufficient to enable efficient PET-degrading activity at moderate temperatures.

SUPPORTING MATERIAL

Six figures and two tables are available at http://www.biophysj.org/biophysj/supplemental/S0006-3495(18)30208-X.

AUTHOR CONTRIBUTIONS

T.F., P.G.-D., M.S., L.P.P., and C.A.R.-S. designed the research. T.F., P.G.-D., and F.E. performed the computational work. P.G.-D. and Y.N. performed the enzyme experiments. P.G.-D. and M.S. solved the crystal structure. T.F., P.G.-D., M.S., L.P.P., and C.A.R.-S wrote the manuscript. M.S., L.P.P., and C.A.R.-S. were leading investigators.

ACKNOWLEDGMENTS

This research was funded by Instituto Antártico Chileno (INACH Regular Grant RG_47-16). P.G.-D. was supported by an American Society for Biochemistry and Molecular Biology PROLAB award. The authors gratefully acknowledge the support of NVIDIA Corporation with the donation of the Titan X and XP GPUs used for this research. M.S. is an Alfred P. Sloan fellow (FR-2015-65794).

REFERENCES

1. McIntyre, J. E. 2004. The historical development of polyesters. *In* Modern Polyesters: Chemistry and Technology of Polyesters and Copolyesters. John Wiley & Sons, Ltd., Chichester, UK, pp. 1–28.
2. Bornscheuer, U. T., D. E. MacArthur, …, J. Muschiol. 2016. Feeding on plastic. *Science*. 351:1154–1155.
3. Sinha, V., M. R. Patel, and J. V. Patel. 2010. Pet waste management by chemical recycling: a review. *J. Polym. Environ.* 18:8–25.
4. Jambeck, J. R., R. Geyer, …, K. L. Law. 2015. Plastic waste inputs from land into the ocean. *Science*. 347:768–770.
5. Wei, R., T. Oeser, and W. Zimmermann. 2014. Synthetic polyester-hydrolyzing enzymes from thermophilic actinomycetes. *Adv. Appl. Microbiol.* 89:267–305.
6. Wei, R., and W. Zimmermann. 2017. Biocatalysis as a green route for recycling the recalcitrant plastic polyethylene terephthalate. *Microb. Biotechnol.* 10:1302–1307.
7. Vertommen, M. A. M. E., V. A. Nierstrasz, …, M. M. C. G. Warmoeskerken. 2005. Enzymatic surface modification of poly(ethylene terephthalate). *J. Biotechnol.* 120:376–386.
8. Nimchua, T., H. Punnapayak, and W. Zimmermann. 2007. Comparison of the hydrolysis of polyethylene terephthalate fibers by a hydrolase from Fusarium oxysporum LCH I and Fusarium solani f. sp. pisi. *Biotechnol. J.* 2:361–364.
9. Liebminger, S., A. Eberl, …, G. M. Guebitz. 2007. Hydrolysis of PET and bis-(benzoyloxyethyl) terephthalate with a new polyesterase from Penicillium citrinum. *Biocatal. Biotransform.* 25:171–177.
10. Yang, S., H. Xu, …, Z. Jiang. 2013. A low molecular mass cutinase of Thielavia terrestris efficiently hydrolyzes poly(esters). *J. Ind. Microbiol. Biotechnol.* 40:217–226.
11. Seman, W. M. K. W., S. A. Bakar, …, F. D. A. Bakar. 2014. High level expression of Glomerella cingulata cutinase in dense cultures of Pichia pastoris grown under fed-batch conditions. *J. Biotechnol.* 184:219–228.
12. Dimarogona, M., E. Nikolaivits, …, E. Topakas. 2015. Structural and functional studies of a Fusarium oxysporum cutinase with polyethylene terephthalate modification potential. *Biochim. Biophys. Acta.* 1850:2308–2317.
13. Müller, R.-J., H. Schrader, …, W.-D. Deckwer. 2005. Enzymatic degradation of poly(ethylene terephthalate): rapid hydrolyse using a hydrolase from T. fusca. *Macromol. Rapid Commun.* 26:1400–1405.
14. Ronkvist, Å. M., W. Xie, …, R. A. Gross. 2009. Cutinase-catalyzed hydrolysis of poly(ethylene terephthalate). *Macromolecules.* 42:5128–5138.
15. Billig, S., T. Oeser, …, W. Zimmermann. 2010. Hydrolysis of cyclic poly(ethylene terephthalate) trimers by a carboxylesterase from Thermobifida fusca KW3. *Appl. Microbiol. Biotechnol.* 87:1753–1764.
16. Chen, S., L. Su, …, J. Wu. 2010. Biochemical characterization of the cutinases from Thermobifida fusca. *J. Mol. Catal., B Enzym.* 63:121–127.
17. Herrero Acero, E., D. Ribitsch, …, G. Guebitz. 2011. Enzymatic surface hydrolysis of PET: effect of structural diversity on kinetic properties of cutinases from Thermobifida. *Macromolecules.* 44:4632–4640.
18. Sulaiman, S., S. Yamato, …, S. Kanaya. 2012. Isolation of a novel cutinase homolog with polyethylene terephthalate-degrading activity from leaf-branch compost by using a metagenomic approach. *Appl. Environ. Microbiol.* 78:1556–1562.
19. Ribitsch, D., E. H. Acero, …, G. M. Guebitz. 2012. A new esterase from Thermobifida halotolerans hydrolyses polyethylene terephthalate (PET) and polylactic acid (PLA). *Polymers.* 4:617–629.
20. Ribitsch, D., E. H. Acero, …, G. M. Guebitz. 2012. Characterization of a new cutinase from Thermobifida alba for PET-surface hydrolysis. *Biocatal. Biotransform.* 30:2–9.
21. Wei, R., T. Oeser, …, W. Zimmermann. 2014. Functional characterization and structural modeling of synthetic polyester-degrading hydrolases from *Thermomonospora curvata*. *AMB Express*. 4:44.
22. Kawai, F., M. Oda, …, M. Tanokura. 2014. A novel Ca2+-activated, thermostabilized polyesterase capable of hydrolyzing polyethylene terephthalate from Saccharomonospora viridis AHK190. *Appl. Microbiol. Biotechnol.* 98:10053–10064.
23. Yoshida, S., K. Hiraga, …, K. Oda. 2016. A bacterium that degrades and assimilates poly(ethylene terephthalate). *Science*. 351:1196–1199.
24. Lenfant, N., T. Hotelier, …, A. Chatonnet. 2013. ESTHER, the database of the α/β-hydrolase fold superfamily of proteins: tools to explore diversity of functions. *Nucleic Acids Res.* 41:D423–D429.
25. Marten, E., R. J. Müller, and W. D. Deckwer. 2005. Studies on the enzymatic hydrolysis of polyesters. II. Aliphatic-aromatic copolyesters. *Polym. Degrad. Stabil.* 88:371–381.
26. Mueller, R. J. 2006. Biological degradation of synthetic polyesters-Enzymes as potential catalysts for polyester recycling. *Process Biochem.* 41:2124–2128.
27. Donelli, I., P. Taddei, …, G. Freddi. 2009. Enzymatic surface modification and functionalization of PET: a water contact angle, FTIR, and fluorescence spectroscopy study. *Biotechnol. Bioeng.* 103:845–856.
28. Donelli, I., G. Freddi, …, P. Taddei. 2010. Surface structure and properties of poly-(ethylene terephthalate) hydrolyzed by alkali and cutinase. *Polym. Degrad. Stabil.* 95:1542–1550.
29. Zumstein, M. T., D. Rechsteiner, …, M. Sander. 2017. Enzymatic hydrolysis of polyester thin films at the nanoscale: effects of polyester structure and enzyme active-site accessibility. *Environ. Sci. Technol.* 51:7476–7485.
30. Sulaiman, S., D. J. You, …, S. Kanaya. 2014. Crystal structure and thermodynamic and kinetic stability of metagenome-derived LC-cutinase. *Biochemistry.* 53:1858–1869.
31. Zhiqiang, L., Y. Gosser, …, J. K. Montclare. 2009. Structural and functional studies of Aspergillus oryzae cutinase: enhanced thermostability and hydrolytic activity of synthetic ester and polyester degradation. *J. Am. Chem. Soc.* 131:15711–15716.
32. Chin, I. S., A. M. A. Murad, …, F. D. A. Bakar. 2013. Thermal stability engineering of Glomerella cingulata cutinase. *Protein Eng. Des. Sel.* 26:369–375.
33. Then, J., R. Wei, …, W. Zimmermann. 2015. Ca 2+ and Mg 2+ binding site engineering increases the degradation of polyethylene terephthalate films by polyester hydrolases from Thermobifida fusca. *Biotechnol. J.* 10:592–598.
34. Shirke, A. N., D. Basore, …, R. A. Gross. 2016. Toward rational thermostabilization of Aspergillus oryzae cutinase: insights into catalytic and structural stability. *Proteins*. 84:60–72.
35. Araújo, R., C. Silva, …, A. Cavaco-Paulo. 2007. Tailoring cutinase activity towards polyethylene terephthalate and polyamide 6,6 fibers. *J. Biotechnol.* 128:849–857.
36. Silva, C., S. Da, …, A. Cavaco-Paulo. 2011. Engineered Thermobifida fusca cutinase with increased activity on polyester substrates. *Biotechnol. J.* 6:1230–1239.
37. Wei, R., T. Oeser, …, W. Zimmermann. 2016. Engineered bacterial polyester hydrolases efficiently degrade polyethylene terephthalate due to relieved product inhibition. *Biotechnol. Bioeng.* 113:1658–1665.
38. Petersen, T. N., S. Brunak, …, H. Nielsen. 2011. SignalP 4.0: discriminating signal peptides from transmembrane regions. *Nat. Methods.* 8:785–786.
39. Otwinowski, Z., and W. Minor. 1997. Processing of X-ray diffraction data collected in oscillation mode. *Methods Enzymol.* 276:307–326.
40. McCoy, A. J., R. W. Grosse-Kunstleve, …, R. J. Read. 2007. Phaser crystallographic software. *J. Appl. Cryst.* 40:658–674.
41. Roth, C., R. Wei, …, N. Sträter. 2014. Structural and functional studies on a thermostable polyethylene terephthalate degrading hydrolase from Thermobifida fusca. *Appl. Microbiol. Biotechnol.* 98:7815–7823.

42. Murshudov, G. N., P. Skubák, …, A. A. Vagin. 2011. *REFMAC* 5 for the refinement of macromolecular crystal structures. *Acta Crystallogr. D Biol. Crystallogr.* 67:355–367.

43. Emsley, P., B. Lohkamp, …, K. Cowtan. 2010. Features and development of Coot. *Acta Crystallogr. D Biol. Crystallogr.* 66:486–501.

44. Bowers, G. N., R. B. McComb, …, R. Schaffer. 1980. High-purity 4-nitrophenol: purification, characterization, and specifications for use as a spectrophotometric reference material. *Clin. Chem.* 26:724–729.

45. Serjeant, E. P., and B. Dempsey. 1979. Ionisation constants of organic acids in aqueous solution. *Int. Union Pure Appl. Chem.* 23:26.

46. Case, D. A., D. S. Cerutti, …, P. A. Kollman. 2017. Amber 2017 Reference Manual: http://ambermd.org/doc12/Amber17.pdf.

47. Maier, J. A., C. Martinez, …, C. Simmerling. 2015. ff14SB: improving the accuracy of protein side chain and backbone parameters from ff99SB. *J. Chem. Theory Comput.* 11:3696–3713.

48. Leaver-Fay, A., M. Tyka, …, P. Bradley. 2011. Rosetta3: an object-oriented software suite for the simulation and design of macromolecules. *Methods Enzymol.* 487:545–574.

49. Hanwell, M. D., D. E. Curtis, …, G. R. Hutchison. 2012. Avogadro: an advanced semantic chemical editor, visualization, and analysis platform. *J. Cheminform.* 4:1–17.

50. Wang, J., W. Wang, …, D. A. Case. 2006. Automatic atom type and bond type perception in molecular mechanical calculations. *J. Mol. Graph. Model.* 25:247–260.

51. Wang, J., R. M. Wolf, …, D. A. Case. 2004. Development and testing of a general amber force field. *J. Comput. Chem.* 25:1157–1174.

52. Jakalian, A., D. B. Jack, and C. I. Bayly. 2002. Fast, efficient generation of high-quality atomic charges. AM1-BCC model: II. Parameterization and validation. *J. Comput. Chem.* 23:1623–1641.

53. O'Boyle, N. M., M. Banck, …, G. R. Hutchison. 2011. Open babel: an open chemical toolbox. *J. Cheminform.* 3:33.

54. Lemmon, G., and J. Meiler. 2012. Rosetta ligand docking with flexible XML protocols. *Methods Mol. Biol.* 819:143–155.

55. Alexander, N. S., A. M. Preininger, …, J. Meiler. 2013. Energetic analysis of the rhodopsin–G-protein complex links the α5 helix to GDP release. *Nat. Struct. Mol. Biol.* 21:56–63.

56. Genheden, S., and U. Ryde. 2015. The MM / PBSA and MM / GBSA methods to estimate ligand-binding affinities. *Expert Opin. Drug Discov.* 10:449–461.

57. Han, X., W. Liu, …, R.-T. Guo. 2017. Structural insight into catalytic mechanism of PET hydrolase. *Nat. Commun.* 8:2106.

58. Heumann, S., A. Eberl, …, G. M. Gübitz. 2006. New model substrates for enzymes hydrolysing polyethyleneterephthalate and polyamide fibres. *J. Biochem. Biophys. Methods*. 69:89–99.

59. Baker, P. J., and J. K. Montclare. 2010. Biotransformations using cutinase. *In* ACS Symposium Series, pp. 141–158.

60. Kawabata, T., M. Oda, and F. Kawai. 2017. Mutational analysis of cutinase-like enzyme, Cut190, based on the 3D docking structure with model compounds of polyethylene terephthalate. *J. Biosci. Bioeng.* 124:28–35.

61. Kitadokoro, K., U. Thumarat, …, F. Kawai. 2012. Crystal structure of cutinase Est119 from Thermobifida alba AHK119 that can degrade modified polyethylene terephthalate at 1.76 Å resolution. *Polym. Degrad. Stabil.* 97:771–775.

62. Benjamin Stranges, P., and B. Kuhlman. 2013. A comparison of successful and failed protein interface designs highlights the challenges of designing buried hydrogen bonds. *Protein Sci.* 22:74–82.

63. Joo, S., I. J. Cho, …, K.-J. Kim. 2018. Structural insight into molecular mechanism of poly (ethylene terephthalate) degradation. *Nat. Commun.* 9:382.

64. Groß, C., K. Hamacher, …, S. Jager. 2017. Cleavage product accumulation decreases the activity of cutinase during PET hydrolysis. *J. Chem. Inf. Model.* 57:243–255.

65. Prompers, J. J., A. Groenewegen, …, H. A. M. Pepermans. 1999. Backbone dynamics of Fusarium solani pisi cutinase probed by nuclear magnetic resonance: the lack of interfacial activation revisited. *Biochemistry.* 38:5315–5327.